Annual Cycle of Pacific–North American Seasonal Predictability Associated with Different Phases of ENSO

ARUN KUMAR

Climate Modeling Branch, NOAA/NCEP/EMC, Washington, D.C.

MARTIN P. HOERLING

Cimate Diagnostics Center, CIRES, University of Colorado, Boulder, Colorado

(Manuscript received 15 September 1997, in final form 28 January 1998)

ABSTRACT

The potential for seasonal mean predictability over the Pacific and North American regions is evaluated as a function of the amplitude of equatorial Pacific sea surface temperature forcing, the phase of that forcing, and the phase of the annual cycle. The potential predictability is measured as the ratio of the seasonal mean SST-forced signal and the internally generated seasonal mean noise. The authors' assessments are derived from the output of ensemble atmospheric general circulation model experiments forced with observed monthly SSTs for 1950–94. Using a perfect prognostic approach, results are presented on the predictability of upper-tropospheric circulation, North American land temperature, and precipitation.

Seasonal predictability is shown to depend on the amplitude of the SST-forced signal, whereas the background noise is largely independent of SSTs. To zero order, that signal grows linearly with the amplitude of anomalous SSTs. An important departure from this is with respect to the phase of tropical Pacific SST anomalies, and the simulated atmospheric signals were stronger for ENSO's extreme warm phases compared to ENSO's extreme cold phases. This asymmetry can be traced throughout the teleconnection chain that links the ENSO forcing region with North American climate.

With regard to the annual cycle's role, the North American climate is shown to be most predictable during the late winter and early spring season of warm events. This stems from the fact that the SST-forced signal during warm events at that time of year is only slightly weaker than in midwinter, whereas the background noise is substantially reduced. Predictability during spring is significantly greater than that occurring in fall, due to a much weaker fall signal. Observational analyses are presented that corroborate these key model results, in particular enhanced skill during ENSO's warm phase and a springtime predictability peak.

Finally, a comparison is made between the classic ratio of variance measure of predictability that commingles all warm, cold, and non-ENSO years to yield a single estimate, against such a ratio calculated for individual events. North American seasonal predictability for specific events can greatly exceed this single gross measure, and it is shown that the latter is a poor yardstick of the prospects for skillful predictions during extreme ENSO states.

1. Introduction

A conventional measure for the expected skill of seasonal climate forecasts involves the ratio of the El Niño–Southern Oscillation (ENSO) climate signal and the background climate noise, and the small value of such a ratio in the extratropics has led to the interpretation that the potential for seasonal predictability is low there (e.g., Madden 1976; Chervin 1986; Kumar and Hoerling 1995; Rowell 1998). The ratio of variances are derived from long time series analysis, using either observed or numerical model data, and the results yield a single estimate of predictability. Such estimates, by spanning all possible sea surface temperature (SST) states, are inherently indiscriminating and offer little guidance on the expected level of atmospheric predictability for individual events. Given that short-term climate forecasts are event based, it becomes critical to step beyond gross measures and understand the predictability limits under specific ENSO scenarios.

Does, for example, the predictability inherent in the climate system differentiate between strong versus weak ENSO events? It is reasonable to presume that climate predictability will be elevated for the stronger events, and this intuition is confirmed by the results of atmospheric general circulation models (AGCMs) (Geisler et al. 1985; Brankovic et al. 1994; Kumar et al. 1996). In a recent study, Kumar and Hoerling (1997) show that the amplitude of the boreal wintertime atmospheric sig-

Corresponding author address: Dr. Martin P. Hoerling, CIRES/Climate Diagnostics Center, University of Colorado, Campus Box 449, Boulder, CO 80309.
E-mail: mph@cdc.noaa.gov

nal during warm events grows quasi-linearly with increased amplitude of the tropical SST forcing. For sufficiently large tropical forcing, such as occurred during 1982–83, the vigor of circulation responses over the Pacific–North American (PNA) region implies a high potential for seasonal predictability (Hoerling and Kumar 1997).

Does the potential predictability of the climate system discriminate between the extreme phases of ENSO? The cold phase of ENSO is known to exert an effect on the PNA region (e.g., Ropelewski and Halpert 1986); however, it is becoming apparent that its impact is not simply the inverse of ENSO's warm phase (e.g., Hoerling et al. 1997; Montroy et al. 1998). Early experiments using low-resolution climate models suggested that the global climate signal associated with cold events may be much weaker than that associated with warm events (Cubash 1985). Recent GCM simulations of the wintertime atmospheric response to equal but opposite signed equatorial Pacific SST anomalies also show the cold event signal to be weaker than its warm event counterpart (Hoerling et al. 1997). These analyses leave the impression of reduced wintertime predictability during cold events.

What is the annual cycle dependency of short-term climate predictability? The winter season has received most of the attention owing to the large extratropical response to ENSO at that time of year. Arguments for greater predictability outside of the winter season have recently been offered, however, and such seasonal variations could result from two sources. On the one hand, for a fixed tropically forced signal, predictability could be enhanced during seasons when the climate noise is reduced (Brankovic et al. 1994). Alternatively, owing to the sensitivity of the extratropical flow to details of the tropical forcing and the appreciable seasonal variations of the ENSO forcing, the extratropical signal itself could be greater outside of winter (e.g., Mitchell and Wallace 1996).

The current study examines the potential for seasonal predictability over the Pacific–North American region by diagnosing the dependence of the atmospheric signal on 1) equatorial SST amplitude, 2) equatorial SST phase, and 3) the annual cycle's phase. In the spirit of conventional signal-to-noise assessments of predictability, this study also examines the variations in climate noise as a function of the amplitude and phase of the SST forcing and as a function of the annual cycle. Our analysis is based on a 13-member ensemble of AGCM simulations forced with the observed monthly global SST variations during 1950–94. The model data and experimental design are described in section 2. Section 3 presents results of the simulated ENSO signal and noise for both tropical and extratropical regions. A detailed assessment of the seasonal predictability over North America is provided in section 4, and concluding remarks and a discussion appear in section 5.

2. Datasets and methods

a. GCM experiments

Monthly mean global SSTs for the 1950–94 period are imposed as evolving lower boundary forcing for a suite of AGCM simulations. For the 1950–81 period, a near-global SST analysis that employs eigenvector reconstruction as described in Smith et al. (1996) is used. For the post-1982 period, a satellite–in situ blended SST analysis based on the method of optimum interpolation as described in Reynolds and Smith (1994) is used.

The atmospheric model, referred to as MRF9 in several previous studies, is identical to the one described in Kumar et al. (1996). Horizontal scales are spectrally represented at T40 resolution (roughly 3° lat × 3° long), and a sigma coordinate system is employed in the vertical that contains 18 levels in the troposphere and the lower stratosphere. Other aspects of the model are discussed in Kumar et al. (1996).

A 13-member ensemble of experiments has been generated. These differ from each other only in the specification of the atmospheric initial conditions, and each realization experiences the same evolving global SST boundary conditions.

b. Measures of signal and noise

An analysis of the climate signal and the climate noise for each season in the 45-yr record is performed using the results from the model simulations.

Let $X_{i\alpha}$ denote the simulated seasonal mean anomaly for the year α and realization i. The ensemble mean anomaly averaged over all realizations is defined as

$$\overline{X}_{\alpha} = \frac{1}{13}\sum_{i=1}^{13} X_{i\alpha}. \tag{1}$$

For a particular year, each ensemble member is subjected to the same SST forcing, and the departures of individual realizations from the ensemble mean arise due to the internal variability, or climate noise. This noise is measured by the mean spread $\overline{Y}_{\alpha}$ averaged over all realizations:

$$\overline{Y}_{\alpha} = \frac{1}{13}\sum_{i=1}^{13} (X_{i\alpha} - \overline{X}_{\alpha})^2. \tag{2}$$

As for the climate signal defined by (1), the climate noise defined by (2) may depend on the particular SST. In the results of section 3, root-mean-square (rms) area averages of the signal and the noise will be presented. If $\langle\ \rangle$ denotes an area average, then the rms of the signal and the noise are defined by $\langle\overline{X}_{\alpha}^2\rangle^{1/2}$ and $\langle\overline{Y}_{\alpha}\rangle^{1/2}$, respectively.

c. Analysis methods

As a concise way to summarize the large volume of model data on signal and noise for all SST states during

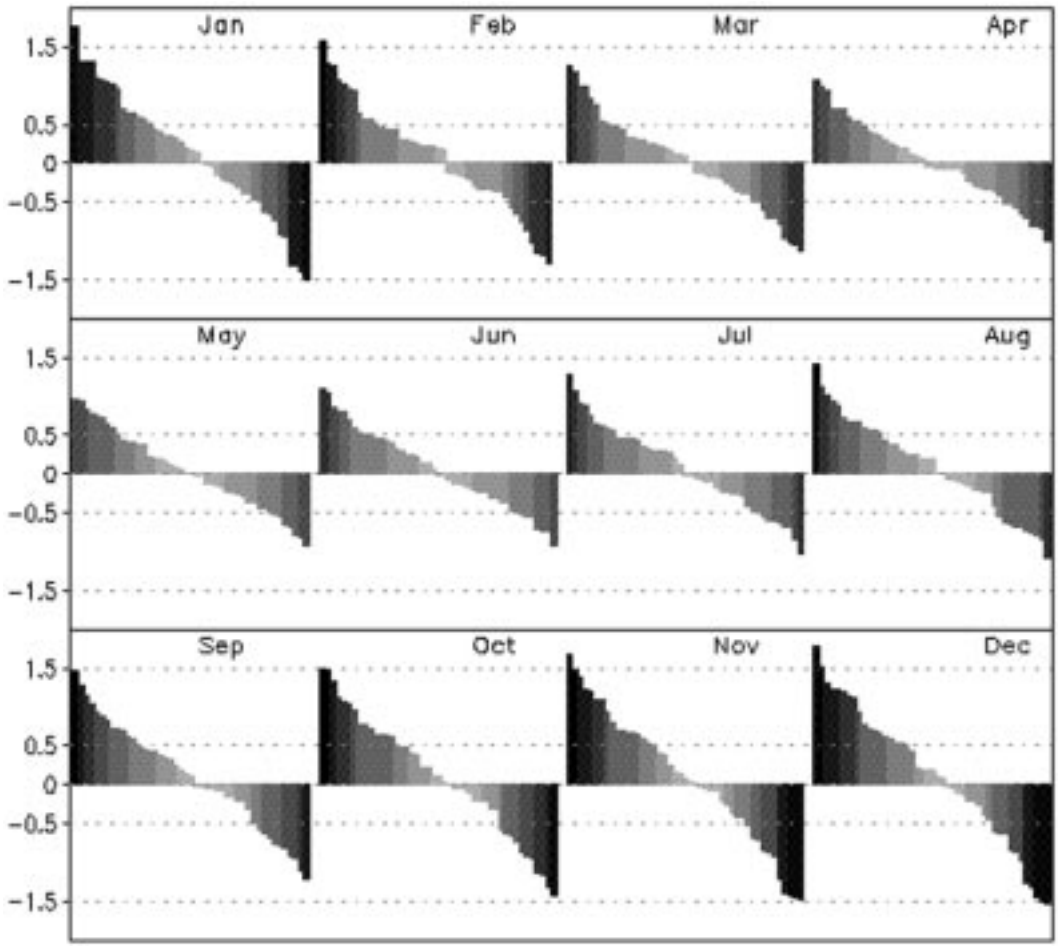

FIG. 1. Seasonal mean sea surface temperature (SST) anomalies during 1950–94 for an area average of the domain 5°N–5°S, 160°E–120°W. Each bar denotes the amplitude of the SST anomaly during the 45-yr record, ranked from the largest warm events on the left-hand side to the largest cold events on the right-hand side. The analysis is performed for each of the 12 overlapping 3-month seasons, and the center month of each season is indicated. Thus, Jan denotes the December, January, February season, etc. Units are °C, shading highlights the magnitude of the SST anomaly.

1950–94, a graphical representation is used as illustrated in Fig. 1. Shown in Fig. 1 is the seasonal variability of the tropical Pacific SST anomalies during 1950–94 for an area average over the spatial domain 5°S–5°N and 160°E–120°W. This area encompasses the entire Niño-4 and the western portion of the Niño-3 index regions. Although not sampling the longitudes of maximum interannual SST variability, the importance of this region lies in the large local sensitivity of deep convection and the resultant forcing of global atmospheric teleconnections. Each bar in the graph corresponds to a 3-month mean, and the individual events have been ranked from the largest warm events on the left-hand side to the largest cold events on the right-hand side. The analysis is repeated for the 12 overlapping seasons beginning with December, January, and February and ending with November, December, and January. It is easily seen that SST anomalies are largest in the northern winter season and that warm and cold events acquire comparable peak amplitudes. The model results in section 3 are also arranged according to the ranked amplitude of the SST anomaly. When displayed in this manner, the dependence of the atmospheric signal and noise on the amplitude and phase of the tropical Pacific SST anomalies is readily identified.

3. Results

A limited set of variables are analyzed to assess ENSO's effect on atmospheric seasonal predictability. These have been chosen to highlight the chain that links the tropical Pacific SSTs and the climate system over the PNA region.

It is important to bear in mind that the results based on the ''perfect-model'' approach used herein will be sensitive to the GCM employed. For example, it is widely recognized that different models have different decompositions of their total seasonal variance into a po-

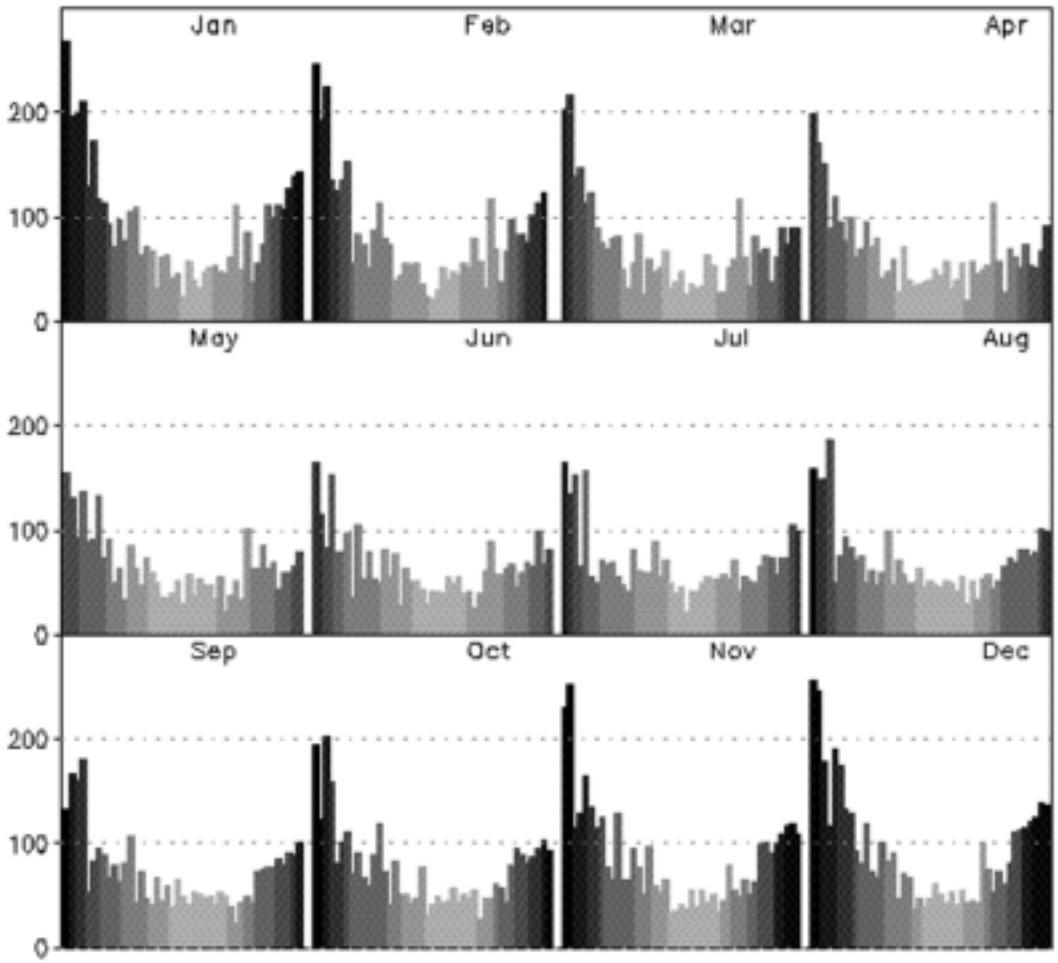

FIG. 2. Root-mean-square (rms) of the ensemble mean AGCM rainfall anomaly during the 1950–94 period. The rms is calculated over the equatorial Pacific domain 5°N–5°S, 160°E–120°W. For each 3-month season indicated, the rms rainfall anomaly is arranged according to the ranked amplitude of the corresponding equatorial Pacific SST anomaly in Fig. 1. Thus, the rainfall corresponding to the warmest SST anomaly appears on the left-hand side, while that for the coldest SST anomaly appears on the right-hand side. Units are mm month^{-1}, and shading highlights the magnitude of the corresponding SST anomaly.

tentially predictable ENSO component and an unpredictable component associated with atmospheric internal dynamics. We have previously analyzed this problem using MRF9 simulations, and based on several different measures of the impact of SST boundary forcing on the extratropics found the model to exhibt realistic ENSO-related wintertime signals over the PNA region. The reader is refered to Kumar et al. (1996) for a detailed assessment of MRF9's seasonal variance.

a. Tropical signal and noise during ENSO

Figure 2 displays the root-mean-square equatorial Pacific rainfall signal area averaged over the domain 5°S–5°N and 160°E–120°W. This is the same region used to analyze the SST anomalies, and as in Fig. 1, the rainfall signals for each season are arranged according to the anomalous SST amplitude. Such a precipitation index is of importance because it represents the first link in the atmospheric response to ENSO, and the amplitude of the index measures the effective atmospheric forcing of teleconnections.

Equatorial central Pacific rainfall is enhanced during warm events and suppressed during cold events for all seasons in the GCM simulations, a response reported in numerous previous empirical and modeling studies. Though to zero order the amplitude of signals in Fig. 2 varies linearly, there are important departures from linearity. Notably, the rainfall signal is not symmetric with respect to extreme phases of ENSO, and strong positive SST anomalies induce larger rainfall signals than do strong negative SST anomalies. This is consistent with observational findings (e.g., Hoerling et al. 1997). Note also that for all seasons the largest rainfall signals during warm events exceed by up to a factor of 2 the largest signals during cold events.

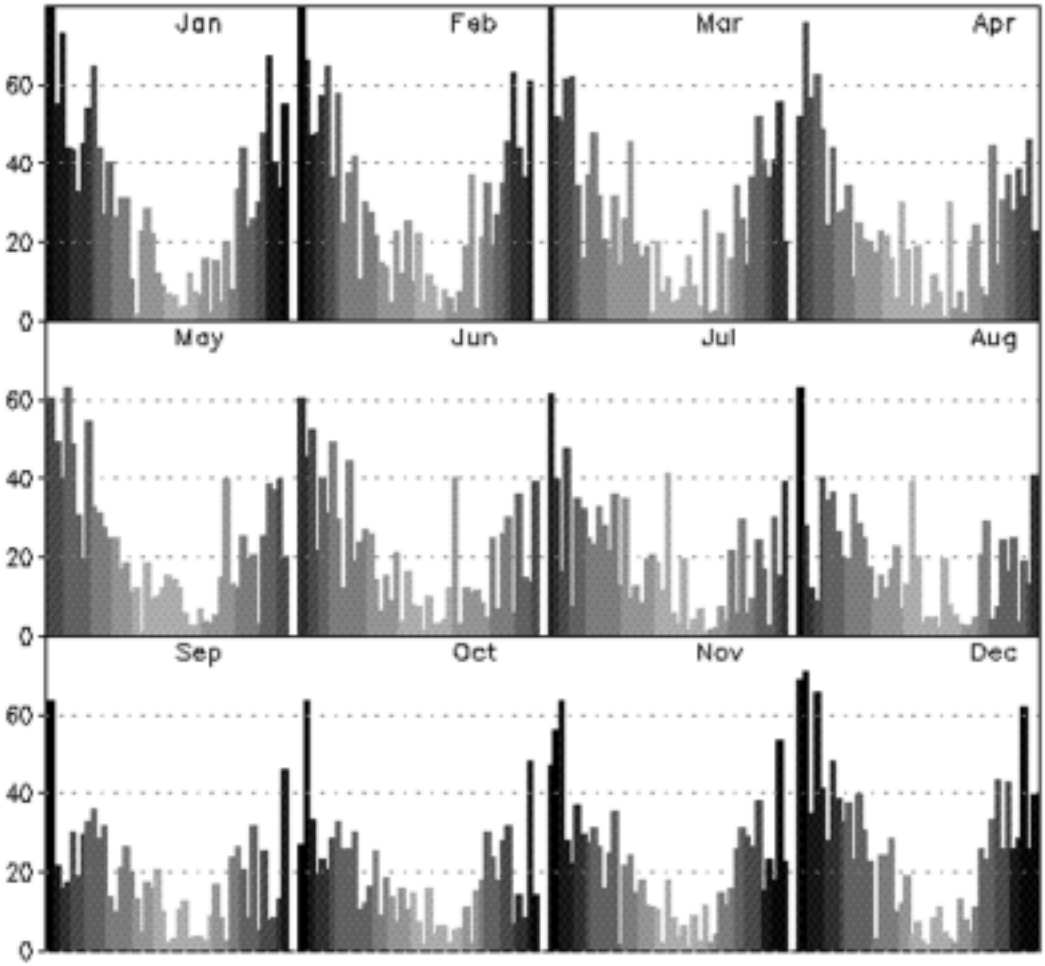

FIG. 3. Same as in Fig. 2, but for the rms of the 200-mb ensemble mean AGCM height anomaly. The rms signal is calculated over the equatorial Pacific domain 5°N–5°S, 160°E–120°W. Units are m.

A related feature of this nonlinear behavior is a saturation effect of the rainfall signal during cold events. In particular, a doubling of the area-averaged cold event SST anomaly from $-0.5°$ to $-1.0°$C is accompanied by little if any further decrease in the rainfall anomaly. This stems from the fact that rainfall is climatologically sparse over the cold tongue region, and a moderate cold event is itself sufficient to entirely suppress convection there. This should be contrasted with warm events where a similar increase of the SST anomalies is accompanied by a near doubling of the positive rainfall anomalies, and little evidence for saturation is found.

Shown in Fig. 3 is the AGCM's simulated equatorial 200-mb-height signal that provides a measure of the initial center-of-action in the atmosphere's wave train response to ENSO. This field can be interpreted as the vertically integrated local atmospheric temperature signal associated with the diabatic heating anomalies during ENSO. Figure 3 illustrates the rms strength of that signal area averaged for the same spatial domain as for the SSTs and the precipitation in Figs. 1 and 2, respectively. The equatorial atmospheric signal increases quasi-linearly with the amplitude of the local SST and local rainfall anomalies. The height signal is not symmetric with respect to ENSO extremes, however, and a larger circulation response occurs for warm SST events. This is consistent with the asymmetric response of the local rainfall.

Figure 4 displays the climate noise in the equatorial Pacific 200-mb heights, and an rms measure of that noise is presented. The noise exhibits no systematic variation with either SST amplitude, SST phase, or with the annual cycle. Although not shown, a similar insensitivity of the climate noise in equatorial rainfall is also found.

It is evident from Figs. 3 and 4 that seasonal predictability of the tropical 200-mb heights is primarily a function of the variations in the strength of the signal. For the larger ENSO events, there is a 10-fold increase of the signal above the noise, and even for SST anomalies associated with weaker ENSO events the signal exceeds by several factors the background noise. The resulting high potential predictability of the tropical

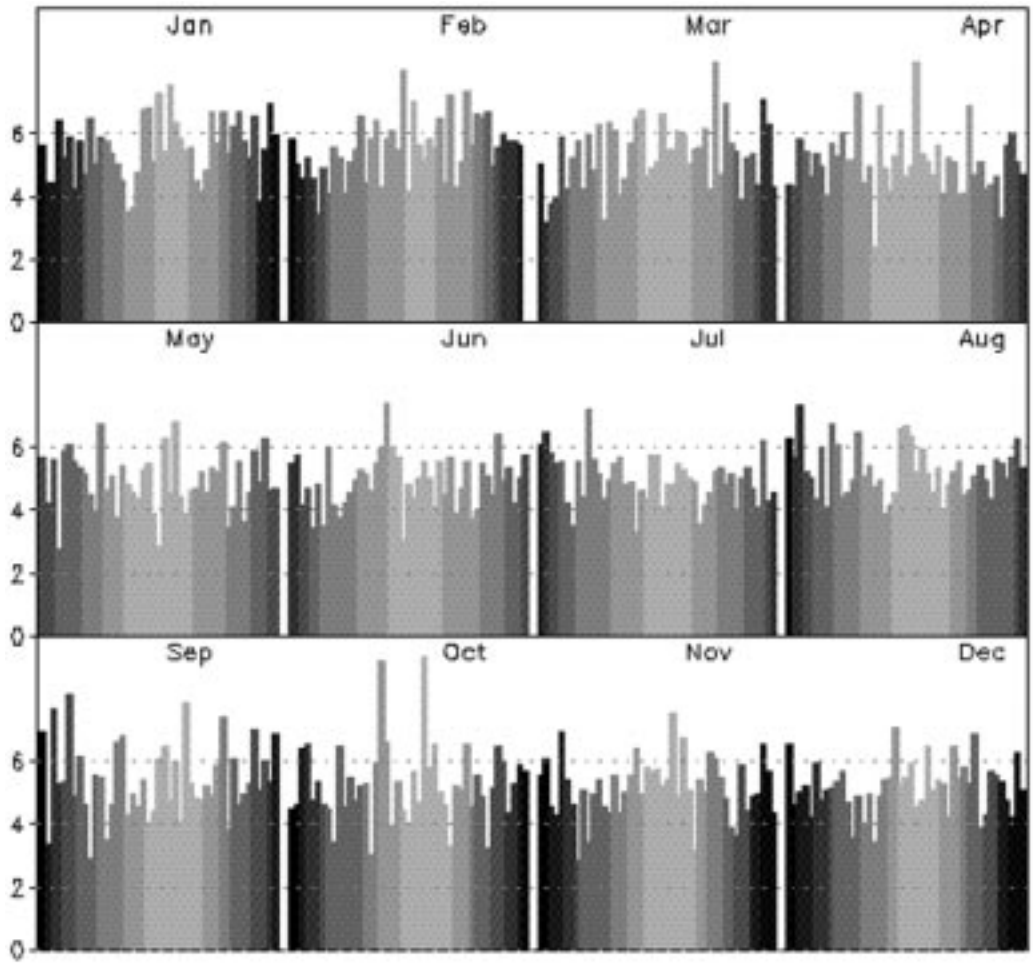

FIG. 4. Root-mean-square (rms) of the AGCM simulated atmospheric noise in 200-mb heights during the 1950–94 period. For a given SST state, the atmospheric noise is defined as the departure of the individual AGCM simulations from the ensemble mean. The rms is calculated over the equatorial Pacific domain 5°N–5°S, 160°E–120°W. For each 3-month season indicated, the rms noise is arranged according to the ranked amplitude of the corresponding equatorial Pacific SST anomaly in Fig. 1. Units are m, and shading highlights the magnitude of the corresponding SST anomaly.

200-mb heights implied by this GCM is consistent with that found in other models (e.g., Lau 1985; Chervin 1986; Stern and Miyakoda 1995). The same high signal-to-noise ratio describes the interannual variations of equatorial central Pacific rainfall.

b. Extratropical signal and noise during ENSO

Linked with the aforementioned tropical circulation anomalies is a characteristic wave pattern whose great circle trajectory leads to centers-of-action over the North Pacific and North American region (Horel and Wallace 1981). We have previously verified the realism of the GCM's composite teleconnection response to ENSO (Kumar et al. 1996) and focus here on the GCM's extratropical signal during each event in 1950–94 separately. This is displayed in Fig. 5 in terms of the rms 500-mb-height anomaly area averaged for the region 20°–70°N and 180°–60°W. Similar results hold for the 200-mb-height field, and the selection of the 500-mb level facilitates comparison with earlier results of Kumar and Hoerling (1997).

The largest signals are once again encountered during warm rather than cold events, and it is evident that the asymmetric equatorial Pacific rainfall response to ENSO extremes (see Fig. 2) manifests itself throughout the teleconnection chain. Furthermore, one can discern a quasi-linear increase of that signal with the SST amplitude. The largest extratropical signals also appear in winter and spring; the summer and fall signals are a factor of 2 weaker, and these exhibit little sensitivity to either the amplitude or the phase of ENSO.

Analagous to the behavior of the signal, a strong seasonal cycle of the climate noise in extratropical 500-mb heights occurs (Fig. 6), although there is no dependency on the anomalous SST state itself. This latter behavior was also found in the Tropics, although the extratropical climate noise is much larger, and consititues a larger

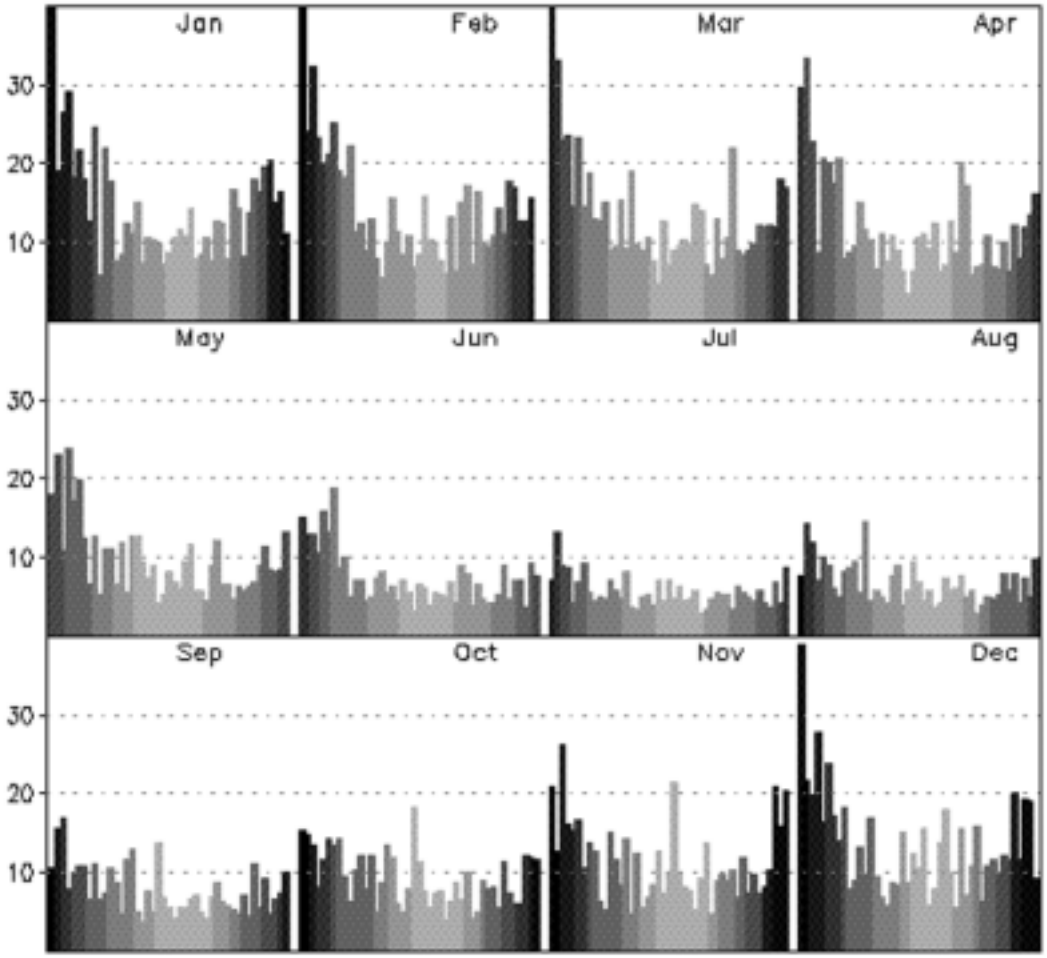

FIG. 5. Same as in Fig. 2, but for the rms signal of the 500-mb ensemble mean AGCM height anomaly. The rms of the signal is calculated over the extratropical Pacific–North American domain defined as 20°–70°N and 180°–60°W. Units are m.

fraction of the overall interannual variability. Indeed, only for the strongest warm events does the signal over the PNA region exceed the noise in the MRF9 simulations. The signal-to-noise ratio and the implied potential predictability in the extratropics will be explored more thoroughly in section 4.

Figure 7 presents the rms measure of the seasonally varying signal in land surface temperature area averaged for the North American domain within 25°–70°N. The sensitivity of the GCM's surface temperature signal to ENSO amplitude, ENSO phase, and the seasonal cycle mimics that previously seen in the 500-mb-height field, a result expected from the well-known equivalent barotropic character of the extratropical response. The asymmetry in the temperature signal between warm and cold events is greatest in winter and early spring during which time the warm events consisently exert a larger effect than do the cold events. There is also an asymmetry in the temperature signal with respect to the phase of the annual cycle. Note, especially for warm events, that the springtime signals (seasons centered on March, April, and May) are comparable to their wintertime counterparts and significantly exceed those occurring in the fall.

Our analysis of the GCM's precipitation signal, presented in Fig. 8, focuses on the northeast Pacific and the adjacent Pacific Coast between 30°–45°N, 160°–120°W. Displacements of the Pacific storm track in this region are known to be an important component of the ENSO response (Held et al. 1989; Hoerling and Ting 1994), and within the teleconnection chain these contribute directly to the enhanced risk of flood or drought over portions of North America. Figure 8 shows the rms rainfall signal, and this possesses many of the same characteristics as the North American temperature response. Thus, the rainfall signal tends to increase for larger ENSO events, although this effect seems to be less linear than found in either the temperature or the 500-mb-height fields. Even exempting the extreme rainfall anomaly simulated for 1982–83 event (far leftmost bar in Fig. 8), the remaining warm event rainfall signals during winter are larger than their cold event counter-

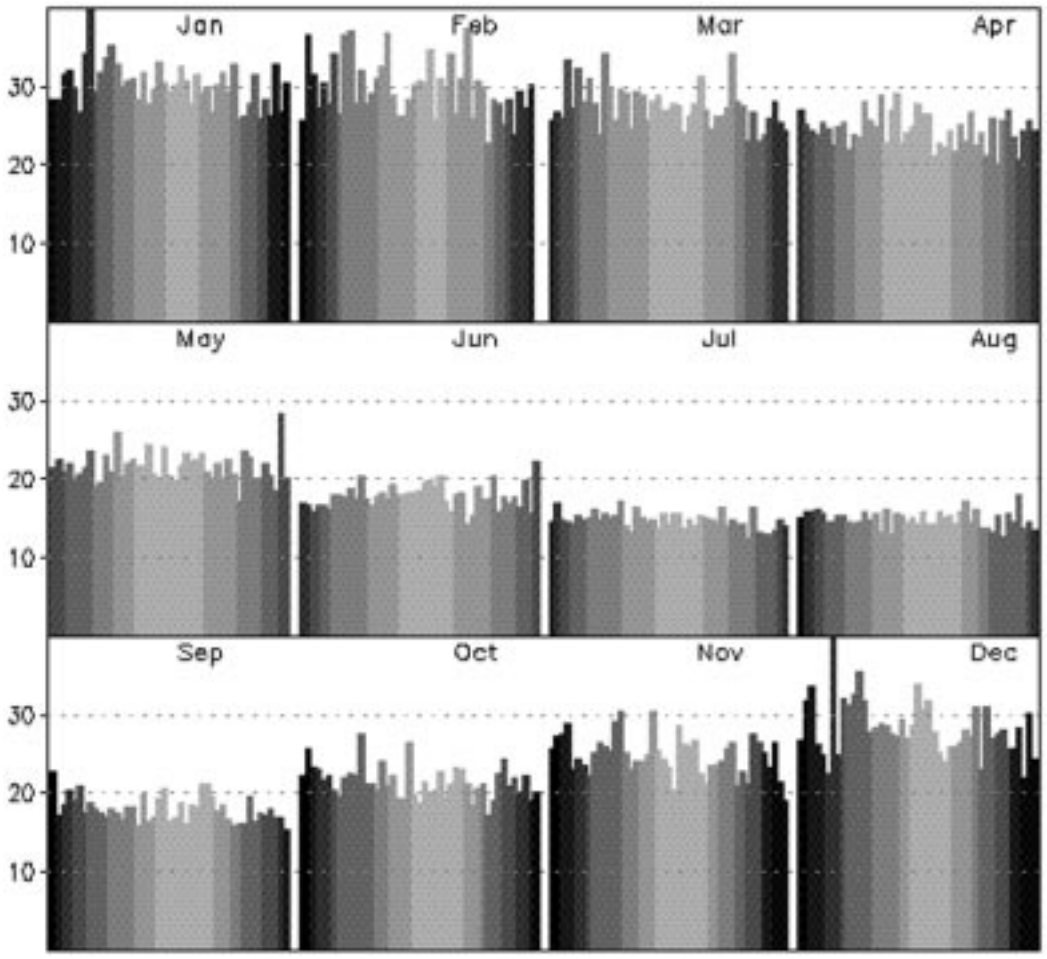

FIG. 6. Same as in Fig. 4, but for the rms noise of the AGCM simulated 500-mb-height anomaly. The rms of the noise is calculated over the extratropical Pacific–North American domain defined as 20°–70°N and 180°–60°W. Units are m.

parts. During the late spring and summer seasons, the GCM's northeast Pacific rainfall shows little sensitivity to ENSO, somewhat in contrast to the distinct late spring signal in simulated North American land temperature.

4. Further assessments of the Pacific–North American seasonal predictability

Using the signal-to-noise ratio as one measure of the potential for seasonal predictability, we illustrate in Fig. 9 the seasonally varying behavior of that ratio for three different variables: PNA sector 500-mb heights, North American land surface temperature, and northeastern Pacific and the adjacent West Coast rainfall. Three scenarios of the seasonal predictability are demonstrated, one based on the average for the three strongest warm events (bold solid curve), another based on the average for the three strongest cold events (thin solid curve), and a third based on the average for all years in 1950–94 (dashed curve). The latter scenario is analogous to the conventional assessment of predictability derived from standard ratio of variance analyses (e.g., Chervin 1986; Kumar and Hoerling 1995; Rowell 1997). Ratios greater than one indicate that the rms signal exceeds the rms noise.

Many of the major points discussed in section 3 are highlighted in Fig. 9. Thus, potential predictability for the strongest warm events consistently exceeds that for the strongest cold events. It is interesting to note that the signal-to-noise ratio for the strongest cold events does not exceed that based on analysis of all years; for both, the signal is generally only half the amplitude of the noise.

Of further importance is the GCM's indication that for warm events maximum potential predictability occurs in late winter to early spring. This result expresses an optimization between the large signal and the modest noise during that time of year. Note also the large asymmetry with respect to the equinox seasons, and the indication of a near doubling of the potential predictability in spring relative to fall during warm events.

An alternate measure of the potential predictability is

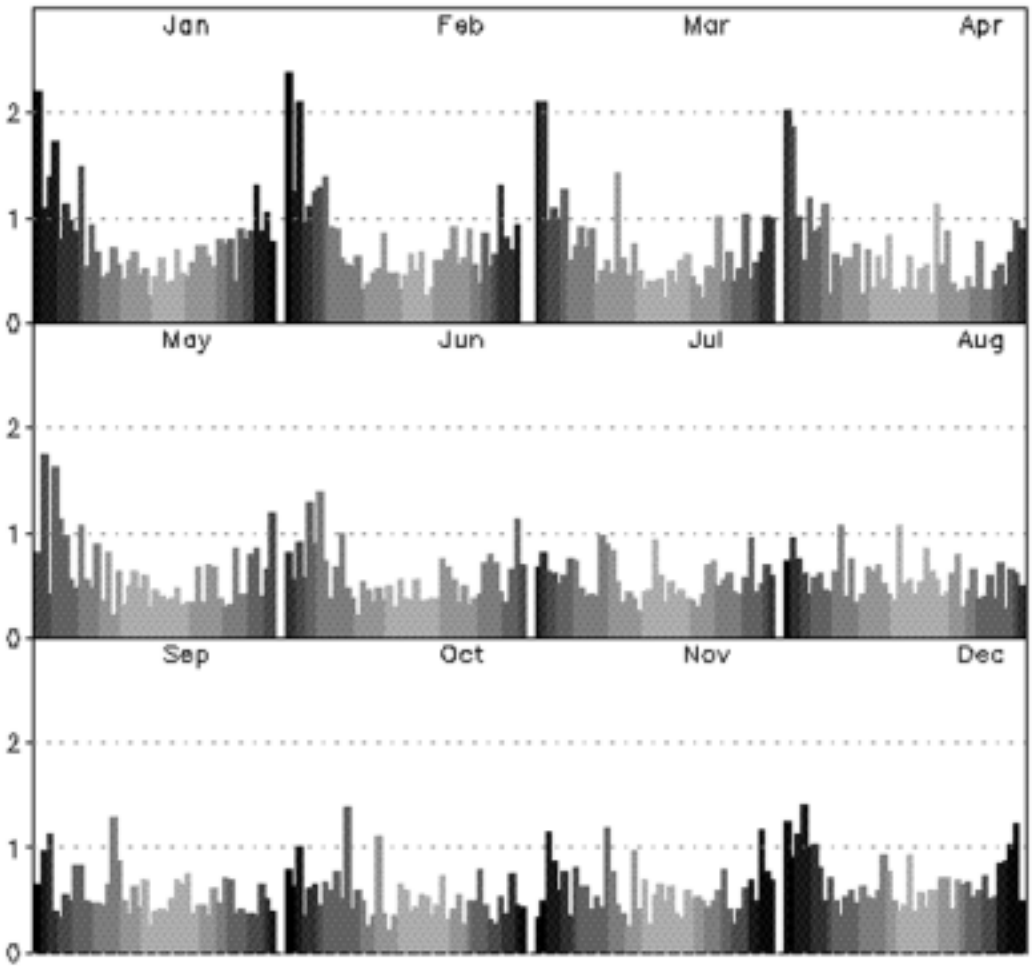

FIG. 7. Same as in Fig. 2, but for the rms signal of the ensemble mean AGCM surface temperature anomaly. The rms of the temperature signal is calculated over the North American land points between 25°–75°N. Units are °C.

the reproducibility of the GCM's spatial anomaly pattern among individual members subjected to identical SST forcing. For any particular season, the reproducibility is estimated from the average of the spatial anomaly correlations between each of the 13 realizations and the ensemble mean signal (e.g., Kumar and Hoerling 1997).

Figure 10 presents the average correlation coefficients of the simulated 500-mb heights for the spatial domain of the PNA region used previously. The ranking is again according to SST amplitude, and all overlapping seasons are shown. The average anomaly correlation increases with the amplitude of tropical Pacific SST anomalies, consistent with analyses of the signal and the noise in Figs. 5 and 6, respectively. A reduced correlation for cold events is apparent; the implied lower skill being symptomatic of a weaker signal during cold events.

The increase in the predictive skill for larger SST anomalies indicated in Fig. 10 is almost entirely due to the increase in the atmospheric signal and not due to a reduction in the internal variability of seasonal means for the more extreme ENSO states (compare also Figs. 5 and 6). Likewise, the GCM's indication of greater skill for warm versus cold events is attributable to the relatively greater warm event signal.

5. Summary and discussion

Optimizing the utility of short-term climate forecasts requires a basic understanding of the expected skill of such predictions. In this study, a perfect prognostic approach has been taken to understand how the skill of seasonal predictions can vary as a function of the amplitude of tropical Pacific SST forcing, the phase of that forcing, and the phase of the annual cycle. Potential predictability at both the surface and the upper troposphere has been assessed, and results focused on the Pacific–North American sector in order to highlight the principal teleconnection chain linking tropical Pacific SSTs and the Northern Hemisphere midlatitudes.

The central equatorial Pacific rainfall signal, as a first link in the teleconnection process, was shown to increase quasi-linearly with the ENSO SST forcing. This

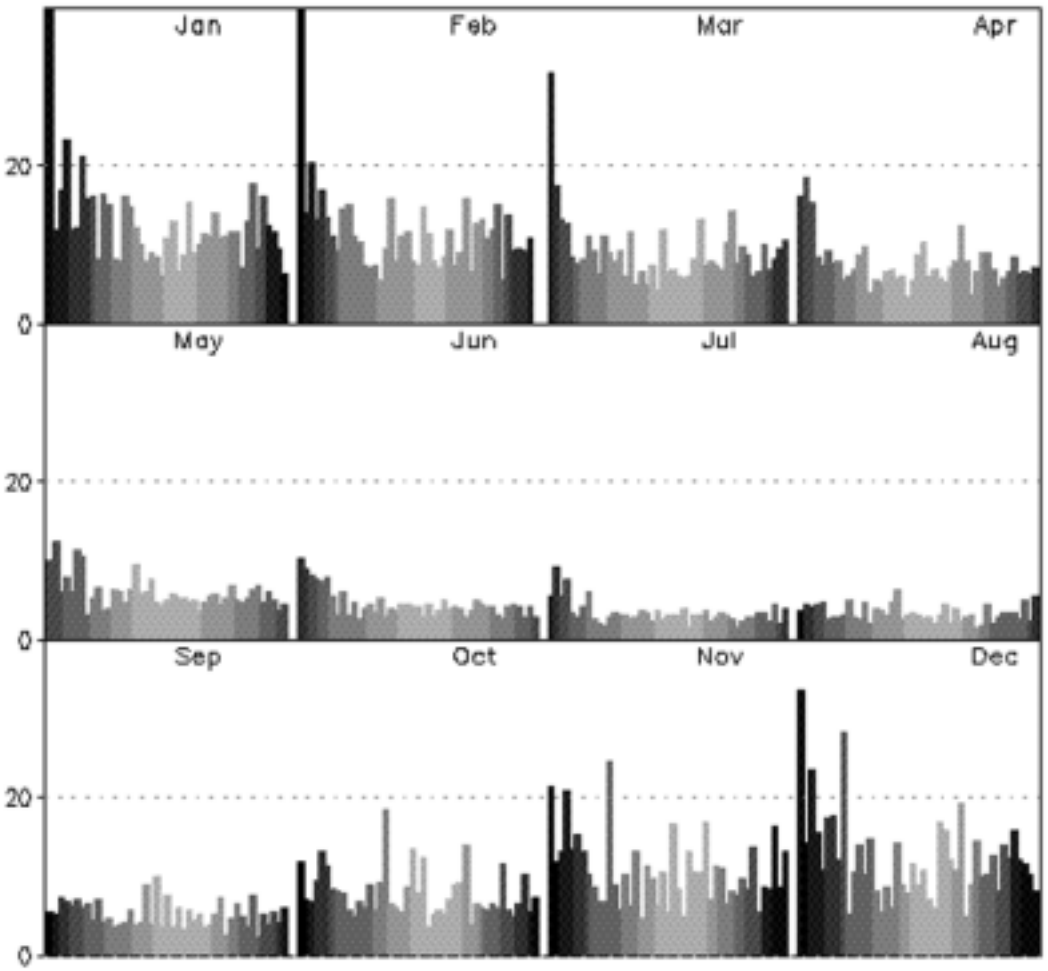

FIG. 8. Same as in Fig. 2, but for the rms signal of the ensemble mean AGCM rainfall anomaly. The rms of the rainfall is calculated for the northeast Pacific region–West Coast domain bounded between 30°–45°N and 160°–120°W. Units are mm month^{-1}.

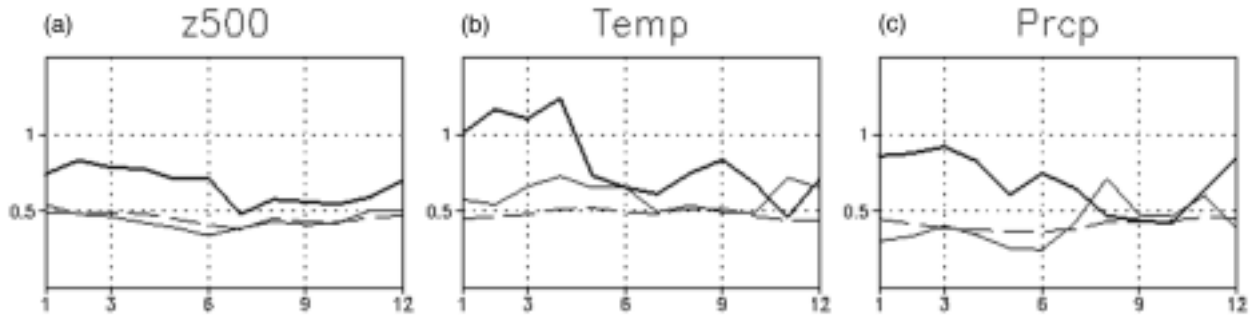

FIG. 9. Seasonal variation of the ratio of the simulated rms signal to the rms noise for (a) 500-mb height over the extratropical Pacific–North American region (left panel), (b) land surface temperature over North America (middle panel), and (c) northeast Pacific–West Coast rainfall (right panel). The ratios are calculated from the average of the three strongest warm events (thick solid contour), the average of the three strongest cold events (thin solid contour), and average over all years in 1950–94 (dashed line). The center month of each season is indicated on the *x* axis by a numeral, with 1 denoting the December, January, February season etc. The spatial domain for the area averages of the 500-mb heights, surface temperatures, and rainfall are identical to those used in Fig. 6, Fig. 7, and Fig. 8, respectively. The ratio is dimensionless.

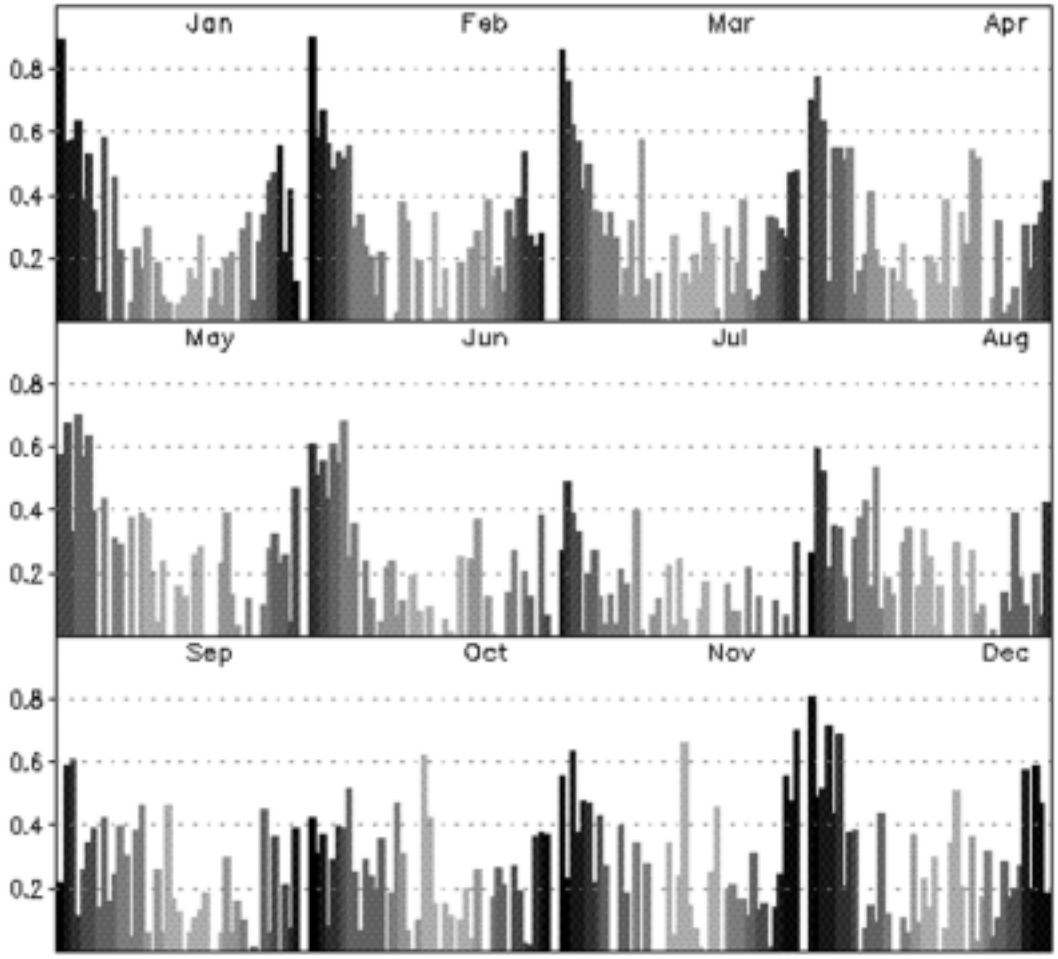

FIG. 10. Spatial 500-mb-height correlations between the AGCM ensemble mean anomaly and the anomalies for individual simulations during 1950–94. For each season, 13 simulations were performed. The spatial correlation of each member for a particular season with the 13-case ensemble average for that season is computed. Correlations are calculated using a cross-validation approach, i.e., the individual AGCM realization is not included in the ensemble mean against which is it correlated, and the average correlation coefficient is plotted. The spatial correlation is calculated over the PNA region defined as 20°–70°N, 180°–60°W. For each 3-month season indicated, the average correlations are arranged according to the ranked amplitude of the corresponding equatorial Pacific SST anomaly, and the shading highlights the magnitude of that anomaly. Average correlations below zero are not plotted.

signal exceeded by nearly one order of magnitude the background atmospheric noise, and thus was highly predictable. Consistent with observational analyses of Hoerling et al. (1997), the simulated rainfall signal for warm events exceeded that for cold events. Indeed, beyond a certain negative SST anomaly during cold events, no further reduction in the local rainfall occurred, whereas no such saturation effect was found for warm events.

Such asymmetry in the strength of the atmospheric signal with respect to opposite phases of ENSO emerged throughout the teleconnection chain. Though there was a prevailing linear increase of the teleconnection response with SST amplitude, the warm event signal exceeded the cold event signal by a factor of 2 for the extreme phases of ENSO. In contrast, the background climate noise in the extratropics exhibited no preference for either the phase or the amplitude of ENSO. In other words, the atmospheric perturbations associated with ENSO were found not to alter the internally generated seasonal variations of the extratropical atmosphere. As such, the variations in potential predictability with tropical Pacific SSTs was shown to be a function of the atmospheric signal alone.

That signal was shown to exhibit strong seasonality over the extratropical Pacific and North America. Thus, the winter and spring signals were considerably larger than their summer and fall counterparts. Such seasonal variations were not obviously related to variations in the tropical convective forcing itself; the latter exhibited comparatively little sensitivity to the annual cycle. The stronger winter and spring extratropical signals would

thus appear to be intinsic features of the dynamics of tropical–extratropical interactions.

Using the ratio of the climate signal to the climate noise as one measure of predictability, the late winter/early spring season during warm events was shown to exhibit the greatest potential for skillful predictability over North America. The large asymmetry of potential predictability with respect to the equinox seasons was especially noteworthy, and the simulated ratio of variance in spring was double that occurring in fall.

The intrinsic value of such seasonal variations in atmospheric predictability needs to be weighed against the predictability of tropical Pacific SSTs themselves. There are reasons to suspect that the equatorial Pacific SSTs may not be equally predictable throughout the lifetime of an ENSO event. For example, observations of the temporal evolution of equatorial Pacific SST anomalies during warm events reveal a fairly systematic and reproducible behavior in their growth phase, in contrast to a more variable and outwardly chaotic behavior among events during their sequent decline. This leads to the impression of greater predictability of El Niño SSTs for their late fall peak phase, but reduced predictability for their subsequent springtime decay phase. The extent to which this may be true in ocean prediction systems has yet to be determined.

An important question is whether the GCM captures the ENSO-related sensitivity in the observed climate system. It is well known that GCM biases can distort the underlying sensitivity to forcing, and some climatological features of the GCM used herein have been shown to depart from observations (e.g., Kumar et al. 1996; Livezey et al. 1997). Parallel analyses using ensemble simulations of different GCMs are clearly needed.

Several gross characteristics of the seasonal predictability, however, can be extracted from nature itself. Whereas these measures are necessarily limited by the short observational record, they nonetheless offer useful yardsticks against which to assess the ensemble GCM results. Figure 11 presents an analysis of the annual cycle of the signal-to-noise ratio of the observed 500-mb heights during warm (bold curve) and cold (thin curve) phases of ENSO. The National Centers for Environmental Prediction's 500-mb operational analyses are used for the period 1947–96, and the diagnosis is performed over the Pacific–North American region identical to that in Fig. 9a. The rms of the anomaly based on the composite of the 10 strongest warm and the 10 strongest cold events in the 50-yr record is defined as the signal. The rms noise is estimated from the variability of each ENSO event's circulation anomaly relative to its appropriate 10-case composite. This procedure commingles SST events having somewhat different amplitude and spatial structure, contrary to the analysis of the GCM ensembles where 13-member analogs were available for each event.

Many of the features in Fig. 11 corroborate the key GCM results of Fig. 9. In particular, the largest signal-to-noise ratio is found in the late winter/early spring season during warm events, and this ratio is double its cold event counterpart during the February–March–April season. This is due to a much stronger observed warm event signal in early spring (not shown), as also found in the GCM. The observations also reveal an asymmetry with respect to the equinox seasons during warm events, owing to a stronger signal in spring compared to fall. Our results are consistent with the observational study of Mitchell and Wallace (1996). They find evidence for a stronger ENSO signal in mean tropospheric temperatures in spring compared to fall and attribute the cause to a stronger equatorial rainfall signal in the spring season.

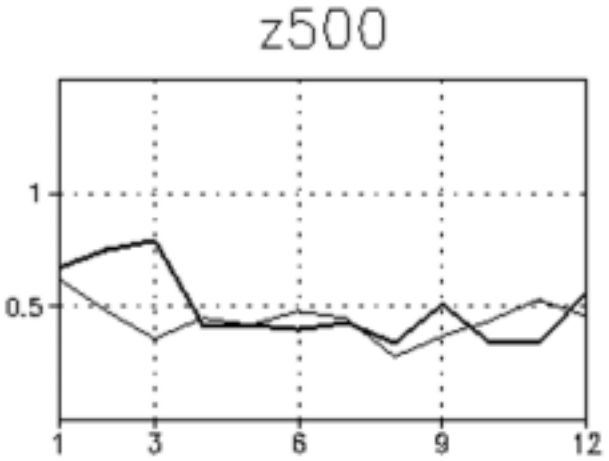

FIG. 11. Observational analysis of the seasonal variation of the ratio of the rms signal to the rms noise for 500-mb height over the extratropical Pacific–North American region. The ratios are calculated from analysis of the 10 strongest warm events (thick solid contour), and the 10 strongest cold events (thin solid contour) in the 1947–96 historical record. Composite height anomalies are calculated for the 10 strongest warm and cold events separately for each season. The signal is estimated from the rms of the composite height anomaly for each 3-month overlapping season. The noise is estimated from the rms of the departure of the individual composite members from its appropriate 10-case composite. The center month of each season is indicated on the *x* axis by a numeral, with 1 denoting the December, January, February season etc. The spatial domain for the area averages of the 500-mb heights is identical to that used in Fig. 9a for the AGCM. The ratio is dimensionless.

Given that seasonal atmospheric predictability over the PNA region depends on both the amplitude and the phase of the tropical Pacific SST anomalies, it follows that decadal variations in those SSTs will yield underlying decadal variations in skill. The lower panel in Fig. 12 illustrates a chronology of the absolute value of central equatorial Pacific SST anomalies from 1950–94, with warm (cold) SST states highlighted in dark (light) shades. Tropical Pacific SST anomalies have exhibited extended quiescent periods, for example from 1959–65 and 1976–82, whereas some periods have witnessed large interannual variations such as during 1968–75 and especially during the post-1982 period. The top panel

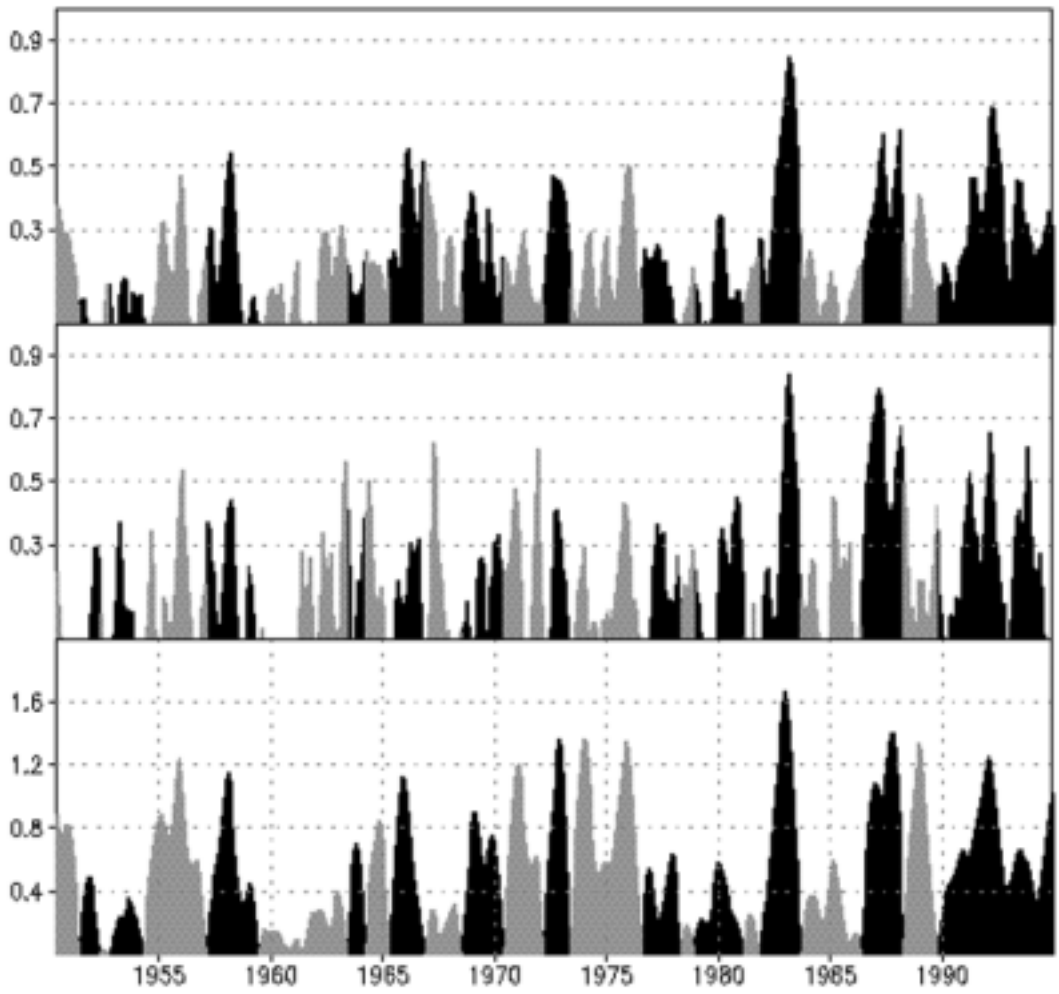

FIG. 12. Time series of the (top panel) average of the spatial 500-mb-height correlations between the AGCM ensemble mean anomaly and the anomalies for the individual AGCM realizations, (middle panel) spatial 500-mb-height correlation between the AGCM ensemble mean anomaly and the observed anomaly, and (bottom panel) absolute value of the area-average equatorial Pacific SST index for the period 1950–94. Spatial correlations are calculated over the extratropical Pacific–North Amerian region as in Fig. 5, whereas the domain for the SST index is as in Fig. 1. In all three panels, the dark shading indicates years with positive SST anomaly while gray shading indicates years with cold SST anomaly. Units for SST anomalies are °C.

of Fig. 12 illustrates a time series of the GCM's atmospheric potential predictability of the PNA-sector 500-mb heights. This figure displays the same results as in Fig. 10, except that here the correlations are plotted chronologically. Note the close correspondence of this time series with that of the SSTs. In particular, 1959–65 is a period of low seasonal predictability, in contrast with the high potential for skillful predictions in the post-1982 era.

A similar result holds when the AGCM ensemble average is spatially correlated with the observed seasonal anomalies, as shown in the middle panel of Fig. 12. Despite the various AGCM biases, and the fact that each observed seasonal anomaly is a blend of signal and noise, a similar low-frequency variability in the correlations can be clearly seen.

The point here is not to suggest an ability to predict decadal climate variations, as that would require an ability to predict the time series of equatorial SSTs on that timescale. Rather, it is to provide a perspective on the recent reports of considerable skill in seasonal atmospheric hindcasts (e.g., Brankovic et al. 1994; Brankovic and Palmer 1997; Kumar et al. 1996; Stern and Miyakoda 1995) based on data of the last decade and the possibility that such predictive skill may be a special feature of the dominance of strong, and predominately warm ENSO events in that period.

Acknowledgments. The support offered by NOAA's Climate Dynamics and Experimental Prediction (CDEP) Program is gratefully acknowledged. We also wish to acknowledge the National Centers for Environmental

Prediction for providing computing facilities as part of the NOAA Seasonal-to-Interannual Climate Prediction Program. The manuscript benefited also from the reviewer suggestions.

REFERENCES

Brankovic, C., and T. N. Palmer, 1997: Atmospheric seasonal predictability and the estimates of ensemble size. *Mon. Wea. Rev.*, **125,** 859–874.

——, ——, and L. Ferranti, 1994: Predictability of seasonal atmospheric variations. *J. Climate*, **7,** 217–237.

Chervin, R. M., 1986: Interannual variability and seasonal climate variability. *J. Atmos. Sci.*, **43,** 233–251.

Cubash, U., 1985: The mean response of the ECMWF global model to the composite El Niño anomaly in extended range prediction experiments. *Coupled Ocean–Atmosphere Models*, J. Nihoul, Ed., Elsevier Press, 329–344.

Geisler, J. E., M. L. Blackmon, G. T. Bates, and S. Muñoz, 1985: Sensitivity of January climate response to the magnitude and position of equatorial Pacific sea surface temperature anomalies. *J. Atmos. Sci.*, **42,** 1037–1049.

Held, I. M., S. W. Lyons, and S. Nigam, 1989: Transients and the extratropical response to El Niño. *J. Atmos. Sci.*, **46,** 163–174.

Hoerling, M. P., and M. Ting, 1994: Organization of extratropical transients during El Niño. *J. Climate*, **7,** 745–766.

——, and A. Kumar, 1997: Origins of extreme climate states during the 1982–83 ENSO winter. *J. Climate,* **10,** 2859–2870.

——, ——, and M. Zhong, 1997: El Niño, La Niña, and the nonlinearity of their teleconnections. *J. Climate,* **10,** 1769–1786.

Horel, J. D., and J. M. Wallace, 1981: Planetary-scale atmospheric phenomenon associated with the Southern Oscillation. *Mon. Wea. Rev.*, **109,** 2080–2092.

Kumar, A., and M. P. Hoerling, 1995: Prospects and limitations of seasonal atmospheric GCM predictions. *Bull. Amer. Meteor. Soc.,* **76,** 335–345.

——, and ——, 1997: Interpretation and implications of observed inter-El Niño variability. *J. Climate,* **10,** 83–91.

——, ——, M. Ji, A. Leetmaa, and P. D. Sardeshmukh, 1996: Assessing a GCM's suitability for making seasonal predictions. *J. Climate*, **9,** 115–129.

Lau, N.-C., 1985: Modeling the seasonal dependence of the atmospheric response to observed El Niños in 1962–76. *Mon. Wea. Rev.*, **113,** 1970–1996.

Livezey, R. E., M. Mautani, A. Leetmaa, H. Rui, M. Ji, and A. Kumar, 1997: Teleconnective response of the Pacific–North American region atmosphere to large central equatorial Pacific SST anomalies. *J. Climate*, **10,** 1787–1820.

Madden, R. A., 1976: Estimates of the natural variability of time-averaged sea-level pressure. *Mon. Wea. Rev.*, **104,** 942–952.

Mitchell, T. P., and J. M. Wallace, 1996: ENSO seasonality: 1950–78 versus 1979–92. *J. Climate,* **9,** 3149–3161.

Montroy, D. L., M. B. Richman, and P. J. Lamb, 1998: Observed nonlinearities of monthly teleconnections between tropical Pacific sea-surface temperature anomalies and central and eastern North American precipitation. *J. Climate,* **11,** 1812–1835.

Reynolds, R. W., and T. A. Smith, 1994: Improved global sea surface temperature analysis using optimum interpolation. *J. Climate,* **7,** 929–948.

Ropelewski, C. F., and M. S. Halpert, 1986: North American precipitation and temperature patterns associated with the El Niño/Southern Oscillation (ENSO). *Mon. Wea. Rev.*, **114,** 2352–2362.

Rowell, D. P., 1998: Assessing potential seasonal predictability with an ensemble of multidecadal GCM simulations. *J. Climate,* **11,** 109–120.

Smith, T. M., R. W. Reynolds, R. E. Livezey, and D. Stokes, 1996: Reconstruction of historical sea surface temperatures using empirical orthogonal functions. *J. Climate*, **9,** 1403–1420.

Stern, W., and K. Miyakoda, 1995: Feasibility of seasonal forecasts inferred from multiple GCM simulations. *J. Climate,* **8,** 1071–1085.